Journal of Materials Chemistry C

ROYAL SOCIETY OF CHEMISTRY

PAPER

View Article Online
View Journal

Check for updates

Cite this: DOI: 10.1039/d5tc04124d

Mechanistic insights into the nitrogen photofixation reaction by BiOBr-based heterojunctions

Giulia Giovilli,[a] Francesca Merlo,[a] Andrea Olivati,[b] Myriam Chems,[a] Andrea Speltini,[a] Michele Loriso,[c] Silvia Colella,[d] Andrea Listorti,[e] Alessandro Landi,[f] Andrea Peluso,[f] Antonella Profumo,[a] Mirko Prato,[g] Julia Wiktor,[h] Annamaria Petrozza,[b] Francesco Ambrosio *[c] and Lorenzo Malavasi *[a]

Received 20th November 2025,
Accepted 3rd February 2026

DOI: 10.1039/d5tc04124d

rsc.li/materials-c

Photocatalytic nitrogen fixation (PNF) offers a green route to ammonia synthesis under ambient conditions. We present a scalable synthesis of BiOBr/g-C_3N_4 heterojunctions and identify that the composition with 10 wt% BiOBr achieves ~20 μmol g^{-1} h^{-1} ammonia production—outperforming pristine materials of the heterojunction. Mechanistic investigations reveal that enhanced activity stems from efficient charge separation, supported by time-resolved spectroscopy showing extended carrier lifetimes. DFT calculations reveal that the catalytically active (010) surface of BiOBr exhibits favorable band alignment with g-C_3N_4 and enables downhill electron transfer to the N_2/NH_3 redox level. Crucially, this surface hosts localized electron polarons, which act as reactive sites for nitrogen reduction. In contrast, the (001) surface lacks such features, explaining the reduced performance at higher BiOBr loadings. These findings establish a direct link among surface structure, charge dynamics, and catalytic functions, offering design principles for next-generation photocatalysts for sustainable ammonia production.

Open Access Article. Published on 04 February 2026. Downloaded on 4/9/2026 3:41:24 PM.
This article is licensed under a Creative Commons Attribution-NonCommercial 3.0 Unported Licence.

Introduction

Sustainable ammonia (NH_3) production is a pressing goal for attaining climate and energy security because ammonia is the backbone of nitrogen fertilizers and is also emerging as a potential carbon-free energy carrier.[1–3] However, conventional ammonia synthesis *via* the Haber–Bosch process consumes tremendous amount of fossil energy and emits significant amount of CO_2.[4] This necessitates the development of green ammonia production methods such as electrochemical synthesis, which could be considered a sustainable alternative only if renewable energy is used.[5] On the other hand, photocatalytic nitrogen fixation (PNF), which uses solar energy to drive the reduction of N_2 to NH_3 under ambient conditions, is an attractive sustainable approach.[6–8] By harvesting sunlight to split water and reduce N_2, photocatalysis could drastically reduce the carbon footprint and energy requirement of ammonia synthesis, aligning with the targets of climate change mitigation and renewable energy integration.

Among various photocatalysts explored for N_2 reduction, bismuth oxybromide (BiOBr) has gained attention as a visible-light-responsive semiconductor. BiOBr features a layered matlockite structure composed of $[Bi_2O_2]^{2+}$ layers alternatively stacked with bromide anions. This layered architecture endows BiOBr with a band gap of about 2.7–2.8 eV, which enables the absorption of visible light.[9–12] Moreover, the internal polarization between the bismuth-oxide and halide layers can induce built-in electric fields that promote charge separation.[13] Owing to these properties, pristine BiOBr can efficiently harvest visible photons and has shown activity in photocatalytic oxidation and

[a] Energy and Materials Chemistry Group, Department of Chemistry and INSTM, University of Pavia, Via Taramelli 16, Pavia, 27100, Italy. E-mail: lorenzo.malavasi@unipv.it
[b] Center for Nano Science and Technology@PoliMi, Istituto Italiano di Tecnologia, 20134, Milan, Italy
[c] Dipartimento di Scienze, Università degli Studi della Basilicata, Viale dell'Ateneo Lucano, 10, Potenza, 85100, Italy. E-mail: francesco.ambrosio@unibas.it
[d] CNR NANOTEC – Istituto di Nanotecnologia – c/o Dipartimento di Chimica, Università degli Studi di Bari "Aldo Moro", 70126 Bari, Italy
[e] Dipartimento di Chimica, Università degli Studi di Bari "Aldo Moro", 70126 Bari, Italy
[f] Dipartimento di Chimica e Biologia Adolfo Zambelli, Università di Salerno, Via Giovanni Paolo II, I-84084 Fisciano (SA), Italy
[g] Materials Characterization Facility, Istituto Italiano di Tecnologia, Via Morego 30, 16163 Genova, Italy
[h] Dipartimento di Chimica e Biologia Adolfo Zambelli, Università di Salerno, Via Giovanni Paolo II, I-84084 Fisciano (SA), Italy

Open Access Article. Published on 04 February 2026. Downloaded on 4/9/2026 3:41:24 PM.
This article is licensed under a Creative Commons Attribution-NonCommercial 3.0 Unported Licence.

reduction reactions, with most of the applications in the degradation of organic pollutants under solar irradiation.[14,15] Nonetheless, pristine BiOBr still suffers from intrinsic limitations such as the rapid recombination of photogenerated electron–hole pairs, leading to low quantum efficiencies.[16] These drawbacks hinder its practical performance and present the need for strategies to improve its photocatalytic efficiency.

To overcome the above limitations, recent studies have focused on engineering the electronic structure and interfaces of BiOBr by constructing heterojunctions with other semiconductors or conductive materials.[14–16] Such well-known strategies in the field of photocatalysis have proven particularly effective for enhancing the visible-light activity of BiOBr-based systems. Chang *et al.* reported one of the early successful attempts by coupling BiOBr with graphitic carbon nitride ($g\text{-}C_3N_4$, from now g-CN) to form 3D hierarchical heterostructures for rhodamine B degradation, which demonstrated improved charge separation under visible light due to the formation of a heterojunction.[17] Following this, several other BiOBr-based systems have been investigated by coupling BiOBr with graphene, $\alpha\text{-}Bi_2O_3$, MoS_2, and polyaniline (PANI).[18–21] All these heterojunctions have been tested for the degradation of dyes and showed enhanced photodegradation rates compared with that of pristine BiOBr.

Building on its general photocatalytic promise, BiOBr has more recently been investigated for the challenging reaction of N_2 fixation under mild conditions. In 2016, Li *et al.* first demonstrated that bismuth oxyhalides, such as BiOCl, can drive the reduction of N_2 to NH_3 under illumination, thereby sparking an interest in BiOBr for green ammonia synthesis.[13,21] According to this early study, BiOBr offers a favorable band structure for this reaction: its conduction band is sufficiently negative to reduce N_2 to NH_3 (thermodynamically), while its valence band can oxidize water to supply protons.[21] However, BiOBr alone shows only modest nitrogen photofixation activity since N_2 molecules adsorb weakly on BiOBr surfaces, leading to inefficient $N\equiv N$ activation and low NH_3 yields.[22] It is well known, in fact, that nitrogen absorption requires the presence of vacancy defects in the form, for example, of nitrogen or oxygen vacancies.[6,7,23] Recognizing these issues, researchers have turned to the surface and interface engineering of BiOBr to improve N_2 reduction efficiency. Oxygen vacancies and surface defect engineering have been employed to strengthen N_2 chemisorption on BiOBr, while cocatalysts (such as noble metals or transition metal sites) have been added to activate N_2 at the surface.[22] In addition, BiOBr-based heterojunctions have been designed to facilitate charge separation and provide energetically favorable pathways for photocatalytic N_2 conversion into ammonia.[8,24,25] Yang *et al.* (2022) reported that constructing Z-scheme heterojunctions with BiOBr can greatly improve nitrogen photofixation. For example, a direct Z-scheme $BiOBr/Bi_4O_5Br_2$ catalyst showed superior NH_3 yields compared to pure BiOBr owing to more efficient charge carrier separation and retention of strong redox power in the Z-scheme system.[26] Such heterojunctions mitigate electron–hole recombination losses and ensure that enough energetic electrons reach the catalyst surface to activate N_2 molecules. Among the potential semiconductors to be coupled to BiOBr, g-CN has been considered because of its good visible light absorption, high stability, and ease of preparation. Recently, Gao *et al.* constructed a tubular g-CN/BiOBr heterojunction that achieved an enhanced ammonia production rate with respect to pristine materials, owing to the close interaction between BiOBr nanospheres grown on the inner and outer surfaces of hollow g-CN nanotubes.[27] However, such an architecture, while efficient for the photocatalytic conversion of nitrogen into ammonia, requires complex synthetic steps, which hinder its scalability potential.[27] Despite these encouraging developments, further improvements in BiOBr-based photocatalysts are needed to meet the demands of efficient green ammonia production.

To further explore the potential of BiOBr-based heterojunctions for the photocatalytic N_2 reduction reaction and attempt to elucidate the reaction mechanism, we investigated the BiOBr/g-CN nanosheets system by exploring the full compositional range between the two semiconductors. Through combined experimental and computational modelling, we uncover how interfacial charge dynamics, band alignment, and surface reactivity govern the observed performance trends. Our findings reveal an optimal composition that maximizes ammonia production while minimizing the BiOBr content, offering new insights into the design principles for efficient and sustainable photocatalysts.

Results and discussion

The BiOBr/g-CN nanosheets system was synthesized according to the experimental procedure reported in the SI, which is schematically represented in Fig. 1. The weight ratios between the BiOBr and g-CN investigated are (wt% of BiOBr) 100%, 90%, 75%, 60%, 45%, 30%, 15%, 10%, and 0%. The procedure adopted here to obtain the BiOBr/g-CN nanosheets system is simple, easily scalable and uses cheap precursors for the preparation of g-CN.

The X-ray diffraction (XRD) patterns of the different compositions are reported in Fig. 2a. Fig. 2b and c report the patterns of pristine materials, namely BiOBr (against the calculated diffraction from the reference crystal structure) and g-CN, respectively.

Fig. 2a shows the prominent contribution of BiOBr, which has a higher scattering density than g-CN and dominates the composite patterns for concentrations above 30 wt%. BiOBr (Fig. 2b) exhibits a typical tetragonal crystal structure (space group *P*4/*nmm*) with lattice parameters of about $a = b = 3.916$ and $c = 8.110$ Å. The diffraction pattern of pure g-CN nanosheets (Fig. 2c) shows typical broad peaks around 13° and 28°, corresponding to the (100) and (002) reflections, respectively.[24]

The study of the morphological properties of the samples was carried out by scanning electron microscopy (SEM), and the results are reported in Fig. S1. In particular, we reported the images of the systems showing the best performance in the ammonia photogeneration (see later in the text), namely

 This journal is © The Royal Society of Chemistry 2026

Open Access Article. Published on 04 February 2026. Downloaded on 4/9/2026 3:41:24 PM.
This article is licensed under a Creative Commons Attribution-NonCommercial 3.0 Unported Licence.

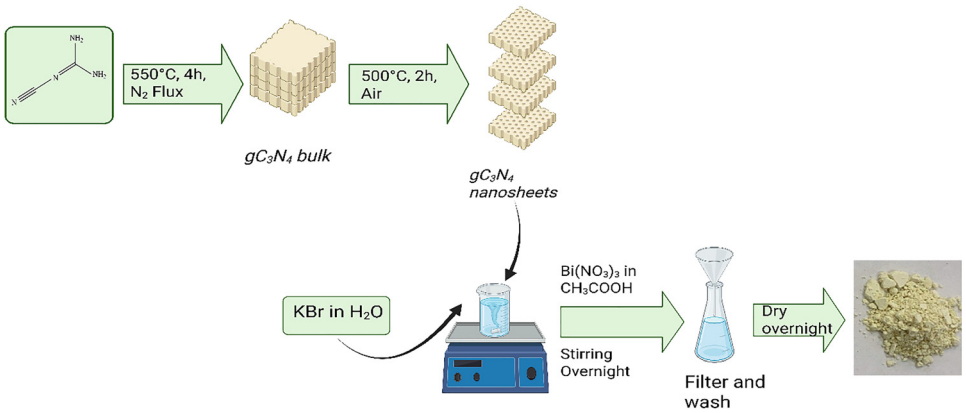

Fig. 1 Schematic of the synthetic procedure to obtain the BiOBr/g-CN sample.

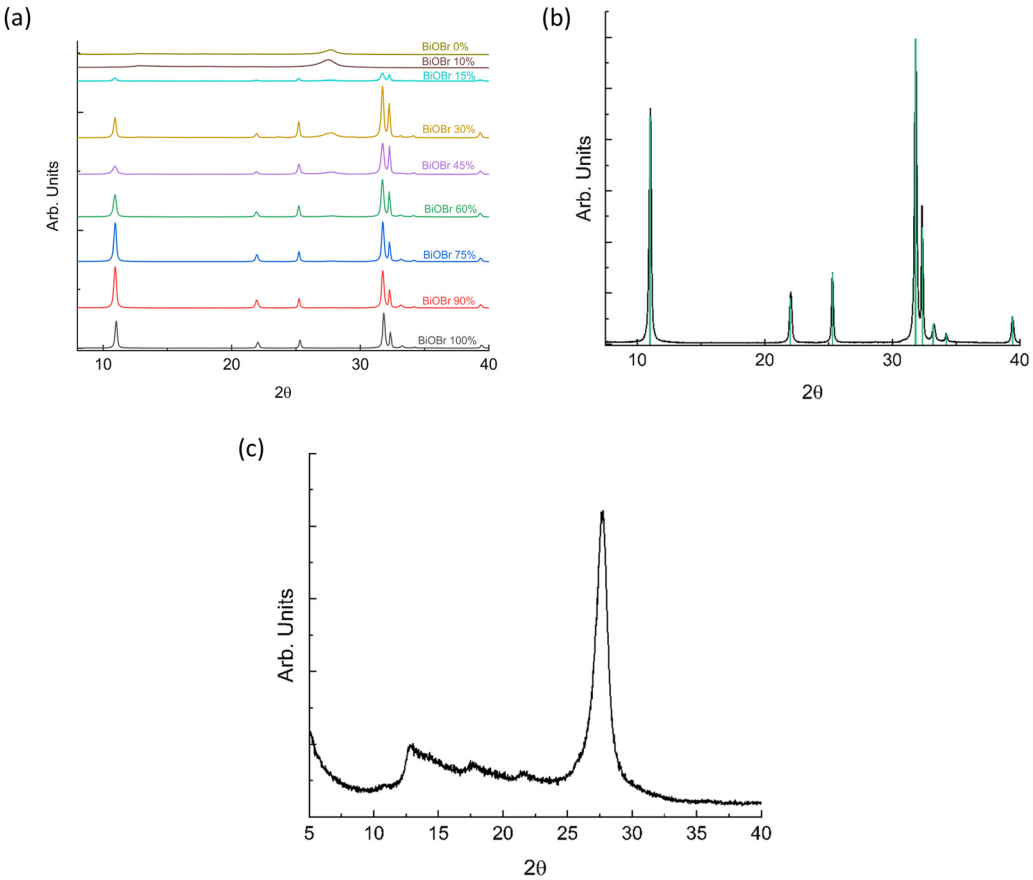

Fig. 2 (a) XRD patterns of BiOBr/g-CN as a function of BiOBr wt%; (b) comparison of the theoretical and calculated XRD patterns of BiOBr; and (c) g-CN diffraction pattern.

those containing 10 wt% of BiOBr with respect to g-CN. A peculiar flower-like morphology is observed for BiOBr (Figure S1a), while this aspect is less evident in the BiOBr/g-CN system. A representative elemental map for BiOBr 10 wt% over g-CN is also reported in the SI (Fig. S1b and c), demonstrating the homogeneous distribution of bismuth oxybromide over g-CN.

UV-Vis absorption spectra and the corresponding Tauc plots for the BiOBr/g-CN system are reported in Fig. S2. The indirect band gap of pure BiOBr is around 2.78 eV, and that of pure g-CN is around 2.70 eV, in agreement with a previous experimental and computational study.[27] Samples with different concentrations of the two semiconductors show slight variations in the band gap energy with intermediate values between the pristine samples in a range of about 0.2 eV without any appreciable trend (reported in Table S1), as expected for a physical mixture forming heterojunctions. In addition, when

Open Access Article. Published on 04 February 2026. Downloaded on 4/9/2026 3:41:24 PM.
This article is licensed under a Creative Commons Attribution-NonCommercial 3.0 Unported Licence.

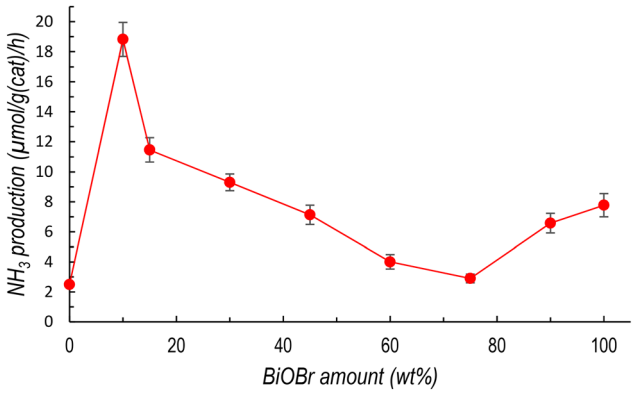

Fig. 3 Ammonia production as a function of BiOBr wt% in the composites. (n = 3, RSD ≤ 10%, simulated solar light, 500 W m^{-2}).

coupling BiOBr with g-CN, the spectra exhibit a gradual increase in sub-band-gap absorption extending toward longer wavelengths. This low-energy absorption tail is characteristic of g-CN and is commonly associated with its low crystallinity, structural disorder, and the presence of localized states. Importantly, the overall position of the absorption edge remains largely unchanged across compositions (Table S1), indicating that the formation of the heterojunction does not lead to a significant modification of the intrinsic band gaps of both semiconductors but primarily affects the density of sub-gap states contributing to visible-light absorption.[14,28,29]

Fig. 3 reports the results in terms of ammonia evolution rates, expressed in μmol g^{-1} h^{-1}, obtained *via* photocatalytic experiments under simulated solar light. Experimental details are provided in the SI for both the photocatalytic experiments and ammonia determination. These were done using an ammonia ion-selective electrode (ISE), which guarantees accurate detection over colorimetric methods.[24,25,30]

The trend of the ammonia evolution rate steeply increases from pure g-CN (about 3 μmol g^{-1} h^{-1}) to the composite containing BiOBr 10 wt%/g-CN 90 wt%, reaching the highest value of about 20 μmol g^{-1} h^{-1}. This value then progressively reduces by increasing the BiOBr amount up to 75 wt% and then increases again, showing effective ammonia photogeneration also for pure BiOBr at a rate of ∼8 μmol g^{-1} h^{-1}.

The data reported in Fig. 3 demonstrate that both the pristine materials exhibit a certain degree of nitrogen reduction activity, with pristine BiOBr performing better than pristine g-CN. The formation of the heterojunction enhances the photocatalytic reduction of nitrogen to ammonia, with the BiOBr (10 wt%)/g-CN (90 wt%) composition showing the best performance. Notably, this is the sample containing the lowest BiOBr loading among those investigated, which represents an important advantage in terms of sustainability of the proposed system. The stability of the ammonia production was tested on the top-performing composites for four successive cycles, as reported in Fig. S3. Post-catalysis XRD and SEM data are shown in Fig. S4, indicating the stability of the system from both a structural and morphological point of view.

The best-performing composition, together with pure BiOBr and g-CN, was investigated by X-ray photoelectron spectroscopy (XPS). Fig. S5 shows the high-resolution spectra collected for the three samples, while Fig. S6 shows the wide-scan spectra. The high-resolution spectra show that the nanoexfoliated g-CN sample is characterized by intense N 1s and C 1s signals, with main peaks centered at (398.8 ± 0.2) eV and (288.3 ± 0.2) eV, respectively, associated with pyridinic N and the carbons in the N–C=N moieties, in line with reports on related systems.[31,32] The BiOBr sample shows intense Bi 4f peaks, with the Bi $4f_{7/2}$ component centered at (159.4 ± 0.2) eV, as well as Br 3d and O 1s signals, with peaks centered at binding energies of (68.5 ± 0.2) eV and (529.9 ± 0.2) eV, respectively. The observed positions are in line with the existing reports on the material.[33] The BiOBr 10 wt%/g-CN 90 wt% sample displays signals of both BiOBr and graphitic carbon nitride. While the signals from g-CN do not show significant variations with respect to the pure sample, a shift of −0.3 eV was observed on the Bi- and Br-related peaks from BiOBr, suggesting that the interaction with g-CN might have induced some electronic rearrangements, with partial electron transfer to BiOBr. This should have induced a partial positive charge on g-CN, which should have resulted in a shift of the XPS signals to a higher binding energy. The large excess of g-CN in the optimized system might have hidden this phenomenon.

To shed light on the different performances of the samples, we first monitored the photoluminescence (PL) of the two pure materials and the heterojunction with the best performance (BiOBr 10 wt%/g-CN 90 wt%).

Fig. 4a shows that the light emission of g-CN is centred at 480 nm and is very weak, while the light emission of BiOBr is at 465 nm. The PL spectrum of the heterojunction, despite its low concentration (BiOBr = 10 wt%), closely resembles that of pure BiOBr.

We monitor the carrier dynamics after light absorption in the different materials using transient absorption spectroscopy measurements. As shown in Fig. 4b and the 2D maps (Fig. 4c and d), at an early time (<1 ns), g-CN and the heterojunction share similar spectra. Both show a broad photobleach signal (red shades) between 520 and 575/675 nm, which corresponds to band edge states filled upon excitation. The difference in the width of this signal, despite a very similar position of the absorption edge, can be related to a different population of defects and distortions, as corroborated by the higher absorption shoulder below the band edge in the case of g-CN compared to the sharper edge of the 10% BiOBr (Fig. 4a) and a higher FWHM of the emission peak (Fig. 4a). At longer wavelengths, it is possible to see a broad and negative photoinduced signal up to 900 nm (blue shades). This negative signal is related to charge carrier transitions promoted after excitation. At longer times (>1 ns), we notice a clear difference between the two samples. For the g-CN sample, the signal turns positive because of the trapping of carriers within the band gap from which they likely recombine non-radiatively. On the other hand, the photoinduced absorption (PIA) signal in the presence of BiOBr lasts up to tens of μs, making the carriers available for

 This journal is © The Royal Society of Chemistry 2026

Open Access Article. Published on 04 February 2026. Downloaded on 4/9/2026 3:41:24 PM.
This article is licensed under a Creative Commons Attribution-NonCommercial 3.0 Unported Licence.

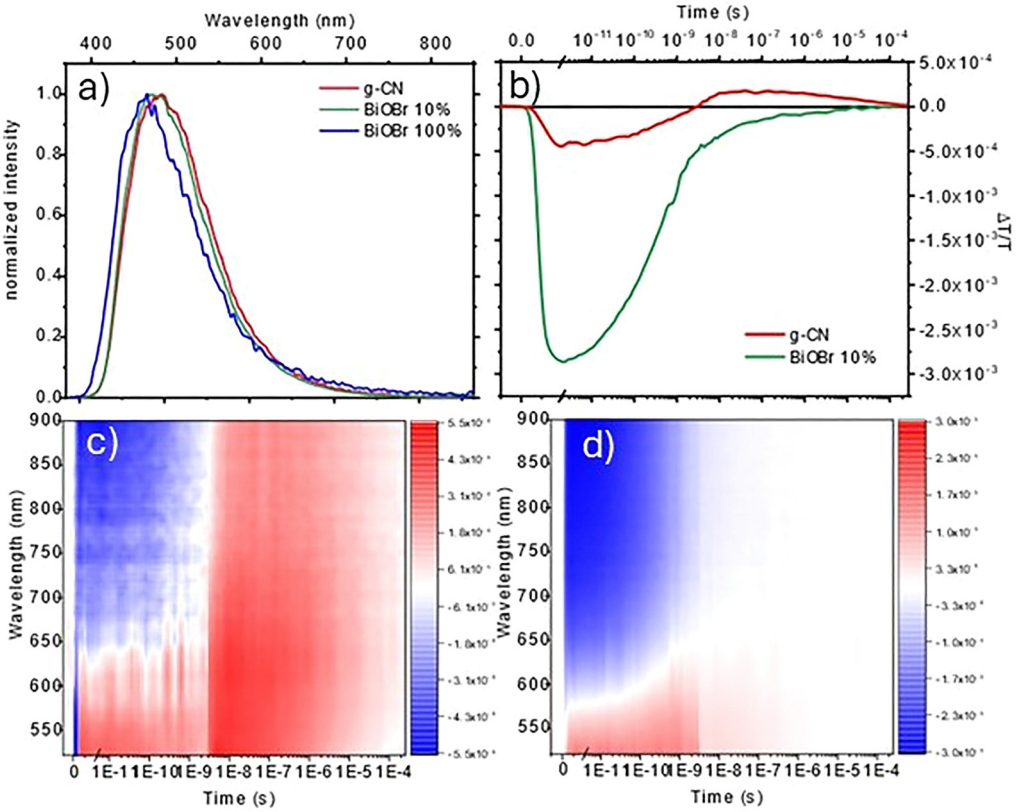

Fig. 4 (a) PL spectra of g-CN (red), BiOBr (blue) and BiOBr 10 wt%/g-CN 90 wt% (green) at 355 nm excitation. (b) Photoinduced absorption dynamics collected between 800 and 900 nm in a time range of up to 250 μs. 2D map representing transient absorption measurements between 520 and 900 nm and in a time range of up to 250 μs: (c) g-CN and (d) BiOBr 10 wt%/g-CN 90 wt%.

a longer time for charge transfer from the photocatalyst to the nitrogen molecule. While the precise microscopic nature of these states cannot be unambiguously identified from TA alone, their long-lived dynamics and correlation with the photocatalytic activity indicate that they act as catalytically relevant intermediates rather than recombination centers. In the case of pure BiOBr (Fig. S7), we observe a really broad positive signal due to the high degree of defect density in this material. It is worth noting that this signal goes to 0 in 20/25 μs, while in the case of CN and the BiOBr/g-CN heterojunction, it lasted to at least 100 μs. Overall, these results confirm, on one side, the formation of the heterojunction and, more importantly, its effective role in making charge carrier dynamics available for the nitrogen reduction reaction, which is evidenced by the clearly prolonged carrier lifetime in the heterojunction, as demonstrated by transient absorption spectroscopy.

In order to get further insights into the photoelectrochemical processes based on the observed NH_3 production, we determine the band alignment for the materials under study. This was conducted *via* advanced electronic-structure calculations based on the piece-wise linear hybrid density functional theory (DFT, *cf.* SI for computational details), which has been found to provide accurate results for large sets of organic, inorganic and hybrid materials.[34–37] The data reported for g-CN are taken from our previous work (ref. 38), whereas here we focus on BiOBr. First, we determine the room-temperature fundamental band gap of the oxyhalide, which is found to be 3.07 eV when accounting for thermal motion at room temperature and spin–orbit coupling (see SI for computational details).[35,38] Considering that exciton binding energies up to 0.1 eV have been measured for BiOBr, the calculated value is in very good accord with the experiment.[39,40] We also note that the band gap reported herein is 0.27 eV larger than a previous theoretical estimate, which was obtained employing a density functional, HSE06, that tends to slightly underestimate the band gaps of Bi-based semiconductors.[41–43]

To study the alignment of the energy levels of the materials under study, we consider two different surface terminations for the band alignment of BiOBr: the bulk-like (001) and (010) surfaces (*cf.* Fig. 5a, the former being approx. four times more stable than the latter (*cf.* SI)). The analysis of the electronic density of states (e-DOS) (*cf.* Fig. 5b, c and Fig. S9) reveals that indeed the (001) surface possesses band edges similar to those of the bulk material: the valence band is mainly constituted by Br 4p states with minor but significant contributions from O 2p and Bi 6s states, while the conduction band has a strong Bi 6p character. The e-DOS for the (010) surface features augmented contributions of Bi states to the band edges due to under-coordinated surface Bi atoms, which suggests an increased reactivity for this system.

Open Access Article. Published on 04 February 2026. Downloaded on 4/9/2026 3:41:24 PM.
This article is licensed under a Creative Commons Attribution-NonCommercial 3.0 Unported Licence.

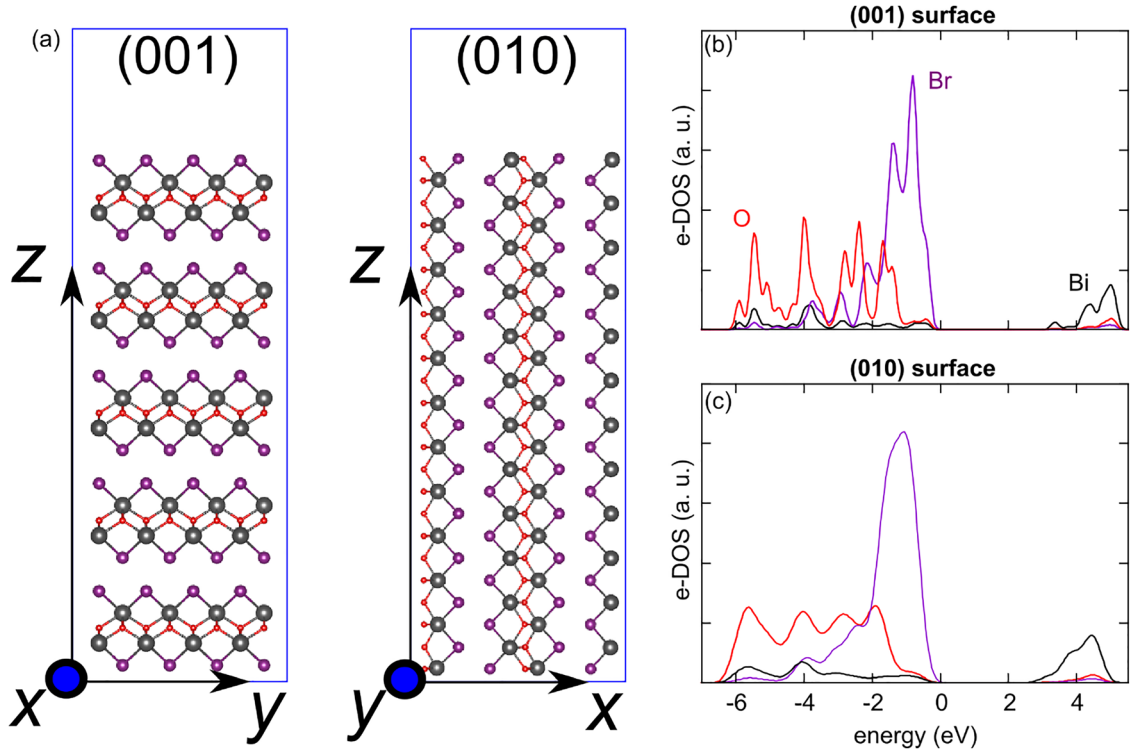

Fig. 5 (a) Ball-and-stick representation of the atomistic models employed to simulate the (010) and (001) surfaces of the BiOX materials. Color codes: O is in red, X = Br, I in purple, and Bi in grey. (b) and (c) Electronic density of states (e-DOS) calculated for the slab models of the (001) and (010) surfaces.

For the (001) surface, our DFT modelling (*cf.* SI) places the valence band maximum (VBM) and conduction band minimum (CBM) 8.07 and 5.00 eV below the vacuum level, respectively, as illustrated in Fig. 6a. This, in conjunction with the corresponding energy levels of g-CN at 6.00 and 3.00 eV *vs.* vacuum, corresponds to a type II alignment for the composite formed by the two semiconductors. This is indeed favorable for charge separation across the interface, as holes are expected to migrate towards g-CN while electrons are transferred to BiOBr. However, we note that the N_2/NH_3 redox level is found to lie 0.23 eV above the CBM of BiOBr, thereby implying a barrier for the reduction reaction, which is not desirable for a swift completion of N_2 fixation. At variance with this, when considering the (010) surface of BiOBr (*cf.* Fig. 6b), the band edges of the oxybromide are found to be pushed closer to the vacuum level, as we calculate the values of the VBM and CBM at 6.51 and 3.44 eV, respectively. Therefore, a suitable band alignment with g-CN is preserved but now with a downhill pathway for N_2 reduction. Considering the inverse exponential dependence of the reaction rate on the energy level difference, this alignment is even more favorable than that of bare g-CN.[44] This result is consistent with the observed better performance of BiOBr with respect to g-CN, when tested individually. Furthermore, the significantly different alignments calculated for (001) and (010) suggest a possible role of the morphology in the composition-dependent performance of the g-CN/BiOBr heterojunctions.

We note that in a previous study on g-CN/$Cs_3Bi_2Br_9$ composites, it was suggested that a similar trend in the photocatalytic production of H_2 could be ascribed to the presence of small electron polarons in the layered perovskite.[47] This, in turn, would be more easily trapped in the bulk region when larger loads of the materials are employed. However, in the present case, it has been demonstrated that electron polarons are unstable in bulk BiOBr, thereby ruling out an analogous explanation of the observed phenomenon.[34] Nevertheless, it has been shown, for different photocatalysts, that charge localization at the surface may be key in boosting the conversion efficiency within unconventional reaction mechanisms.[48] For this reason, we verify the occurrence of electron polarons at the (001) and (010) surfaces by calculating the polaronic energy levels (*cf.* SI). For the (001) surface, we do not find any local distortion leading to surface charge localization: the electron remains delocalized, as in the bulk material (*cf.* Fig. 7a), a result consistent with the passivated nature of the surface.[49] In stark contrast, we observe small polaron formation at the (010) surface (*cf.* Fig. 7b): electron localization is found to occur on undercoordinated surface Bi upon the local distortion of Bi–Br and Bi–O bonds. In particular, a single Bi atom is shifted upwards with respect to the slab plane, a phenomenon which causes an elongation of its bonds by ~0.15 Å, with respect to the neutral system. The polaronic state, found at 0.4 eV below the vacuum level (*cf.* Fig. 7b and SI), may serve as a hotspot for the reduction reaction, in line with previous results on other semiconductors, further supporting the reactivity of the (010) surface.[50,51] Our findings are in line with previous reports on the role of plate-like (010)-dominated BiOBr samples in

 This journal is © The Royal Society of Chemistry 2026

Open Access Article. Published on 04 February 2026. Downloaded on 4/9/2026 3:41:24 PM.
This article is licensed under a Creative Commons Attribution-NonCommercial 3.0 Unported Licence.

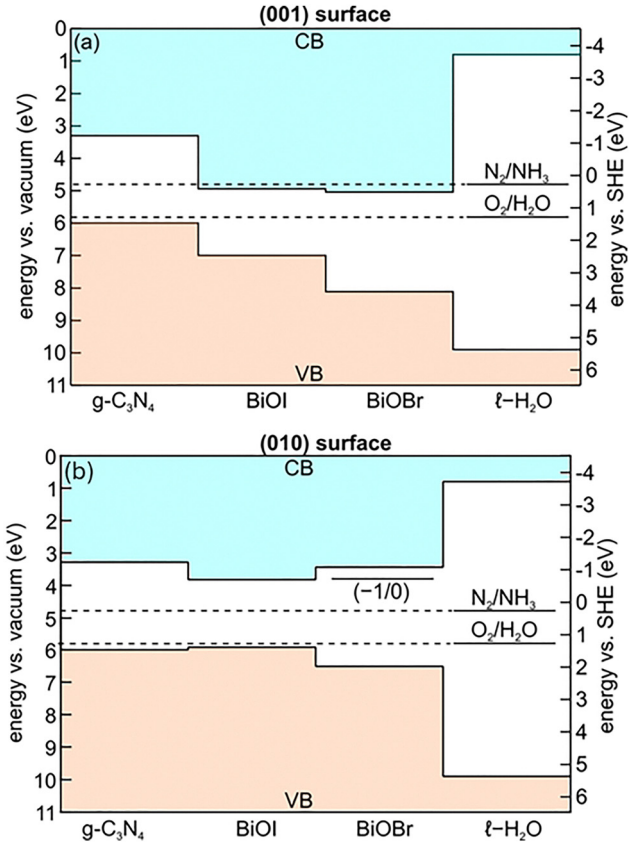

Fig. 6 Valence band (VB) and conduction band (CB) edges of g-CN and BiOX aligned with the band edges of liquid water and with the N_2/NH_3 and O_2/H_2O redox levels through the vacuum level. We also report the energies referred to a computational standard hydrogen electrode developed in ref. 39 and 40.[45,46] Alignment is performed considering the (001) and (010) surfaces of the BiOX semiconductors, as shown in panels (a) and (b), respectively. The (−1/0) charge transition level for the electron at the (010) surface of BiOX is reported in (b). All values are given in eV.

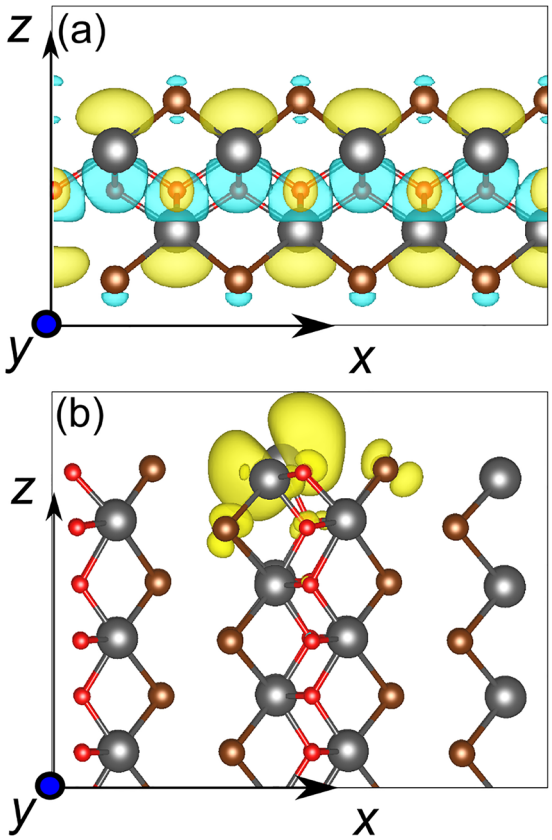

Fig. 7 Isodensity representation of the (a) highest occupied molecular orbital for the negatively charged (001) slab model and (b) spin density associated with the small polaron for the negatively charged (010) slab model. Color codes: Bi atoms in grey, O atoms in red, and Br in bronze.

improving photocatalytic activity with respect to materials featuring (001) domains.[52–57]

Finally, since halide substitution/alloying has been suggested to enhance the efficiency of metal halide perovskites and related materials, we also consider, for comparison, the oxyiodide with an analogous structure, BiOI, for which we calculate a reduced fundamental band gap of 2.06 eV.[58] For the (001) surface, the VBM is found at 7.00 eV, while the CBM is found at 4.94 eV below the vacuum level (*cf.* Fig. 6a). Therefore, the main difference with respect to BiOBr is due to the shift of the VBM of 1.07 eV, while the CBM, which is mainly composed of Bi states, is almost unaffected. The calculated alignment again implies a small energy barrier for the electron transfer reactions associated with N_2 fixation. At variance with this, when considering the (010), as depicted in Fig. 7b, we retrieve a desirable alignment with the N_2/NH_3 redox level. However, the electron polaron is found to be unstable at the (010) surface of BiO, a consequence of the lower energy level of the CBM for the iodide, an instance also observed in other cases, *e.g.* tin halide perovskites.[59] Furthermore, in this case, the alignment with g-CN becomes type I, with both holes and electrons being more stable in the oxyhalide, thereby limiting the efficiency of such a composite. Overall, while Br/I substitution might not be practical in this case, alloying could be a possible strategy to simultaneously achieve a suitable band gap and favorable energy level alignment.

In conclusion, the results of computational modelling suggest that the enhanced reactivity of the composite is promoted by a suitable alignment of energy levels. Furthermore, the composition-dependent trend in ammonia production, which features optimal values for the low loading of BiOBr, can be interpreted with the varying morphology of the system at different wt% values. Indeed, the relative exposure of the more reactive (010) surface – owing to its more favorable band alignment and the presence of surface polarons – compared to the more inert, bulk-like (001) surface may vary as a function of composition. This is in agreement with the diffraction patterns reported in Fig. 2, particularly based on the qualitative evaluation of the intensity ratio between the (110) and (200) to (001) peaks, which are herein considered to support the spectroscopic and modelling results.[60] However, it is important to stress that the role of (010) surfaces may also refer to locally exposed surface motifs within BiOBr domains. Specifically, as

Open Access Article. Published on 04 February 2026. Downloaded on 4/9/2026 3:41:24 PM. This article is licensed under a Creative Commons Attribution-NonCommercial 3.0 Unported Licence.

the (001) surface is sensitively more stable than the (010), nanoparticles are likely to grow preferentially along the former direction. This, in turn, may lead to large domains of poorly reactive (001) surfaces with systems with a larger percentage of the composite. We also note that another possible bottleneck for charge mobility is given by hole polarons, which have been predicted in the bulk.[59] Their reduced mobility, if compared with free charges, might also hinder charge transport across g-CN/BiOX interfaces. Nevertheless, further studies are needed to understand the origin of the promising NH_3 production documented herein, in connection with the reaction mechanism.

Conclusions

In this study, we have systematically investigated the photocatalytic nitrogen fixation performance of BiOBr/g-CN heterojunctions across the full compositional range, prepared *via* a facile, low-cost, and scalable synthetic route. The results demonstrate that coupling these two semiconductors leads to a marked improvement in ammonia production rates under simulated solar light, with the optimal performance achieved for a composition containing 10 wt% of BiOBr. This composite exhibited an ammonia evolution rate of $\sim$20 μmol g^{-1} h^{-1}, nearly seven times higher than that of pristine g-CN and more than twice that of pure BiOBr, while maintaining excellent structural and morphological stability over multiple reaction cycles.

The enhanced activity of the heterojunction can be attributed to improved charge separation and transfer efficiency, as evidenced by photoluminescence quenching, extended carrier lifetimes observed in transient absorption spectroscopy, and band alignment analysis. Density functional theory calculations provided deeper mechanistic insights, revealing that the superior performance could be linked to the exposure of the less stable but more catalytically active BiOBr (010) surface. This surface features favorable energy level alignment with g-CN for downhill electron transfer to N_2, as well as the formation of surface polarons that act as localized electron-rich sites for N_2 activation. In contrast, the more stable BiOBr (001) surface exhibits an energy barrier for nitrogen reduction, explaining the performance drop observed at higher BiOBr loadings where growth along the (001) direction dominates.

The observed synergy between g-CN and BiOBr, especially at a low BiOBr loading, offers a sustainable path by reducing reliance on heavy bismuth content while achieving high activity. Beyond the BiOBr/g-CN system, the mechanistic framework established here—linking facet-dependent band energetics, charge carrier dynamics, and surface polaron formation to catalytic performance—can be extended to the rational design of other heterojunction-based photocatalysts. Ultimately, this work advances our understanding of nitrogen photofixation mechanisms and provides a foundation for the development of efficient, scalable, and environmentally benign routes for solar-driven ammonia production.

Conflicts of interest

There are no conflicts to declare.

Data availability

The data supporting this article have been included as part of the supplementary information (SI). Supplementary information is available. See DOI: https://doi.org/10.1039/d5tc04124d.

Acknowledgements

A.S. acknowledges the funding from PON Ricerca e Innovazione 2014-2020 REACT-EU, DM 1062 2021, project N. 04-G-14266-1. A.L. and L.M. acknowledge financial support under the National Recovery and Resilience Plan (NRRP), Mission 4, Component 2, Investment 1.1, Call for tender No. 104 published on 2.2.2022 by the Italian Ministry of University and Research (MUR), funded by the European Union – NextGenerationEU – Project Title 2022HRZH7P – Re-evolutionary solar fuel production envisioning water stable lead-free perovskite exploitation – REVOLUTION – CUP B53D23015350006 – Grant Assignment Decree No. 1064 adopted on 18.7.2022 by the Italian Ministry of University and Research (MUR). A.P., F.M., M.L. and A.P. acknowledge financial support under the National Recovery and Resilience Plan (NRRP), Mission 4, Component 2, Investment 1.1, Call for tender No. 104 published on 2.2.2022 by the Italian Ministry of University and Research (MUR), funded by the European Union – NextGenerationEU – Project Title ''Towards efficient and cost-effective nitrogen fixation *via* photocatalysis: insights from experiment and theory – PHOTOFIX – CUP F53D23005160006 – Grant Assignment Decree No. 1064 on 18.7.2022 by the Italian Ministry of University and Research (MUR). Francesco Ambrosio and Michele Loriso gratefully acknowledge PRIN 2022-PNRR grant (P2022W9773) for funding. F.A. and M.L. also acknowledge the CINECA award under the ISCRA initiative for providing high-performance computing resources: projects MHP-DEF. AP and AO thank the ''Technologies for Sustainability'' Flagship program of the Istituto Italiano di Tecnologia (IIT). LM acknowledges the Ministero dell'Ambiente e della Sicurezza Energetica (SOLE-H2, Project RSH2A_000004 – CUP: F57G25000080006, funded by European Union – NextGenerationEU, Piano Nazionale di Ripresa e Resilienza (PNRR) Missione 2 Componente 2 Investimento 3.5 – D.D. 279 05/08/2025).

References

1 C. W. Ong, N. Chang, M.-L. Tsai and C.-L. Chen, *Fuel*, 2024, **360**, 130627.
2 B. Wang, T. Li, F. Gong, M. H. D. Othman and R. Xiao, *Fuel Process. Technol.*, 2022, **235**, 107380.
3 E. Spatolisano, L. A. Pellegrini, A. R. De Angelis, S. Cattaneo and E. Roccaro, *Ind. Eng. Chem. Res.*, 2023, **62**, 10813–10827.
4 C. Smith, A. K. Hill and L. Torrente-Murciano, *Energy Environ. Sci.*, 2020, **13**, 331–344.

 This journal is © The Royal Society of Chemistry 2026

Open Access Article. Published on 04 February 2026. Downloaded on 4/9/2026 3:41:24 PM. This article is licensed under a Creative Commons Attribution-NonCommercial 3.0 Unported Licence.

5 N. Bora, A. Kumar Singh, P. Pal, U. Kumar Sahoo, D. Seth, D. Rathore, S. Bhadra, S. Sevda, V. Venkatramanan, S. Prasad, A. Singh, R. Kataki and P. Kumar Sarangi, *Fuel*, 2024, **369**, 131808.
6 S. Chen, D. Liu and T. Peng, *Sol. RRL*, 2021, **5**, 2000487.
7 X. Chen, N. Li, Z. Kong, W.-J. Ong and X. Zhao, *Mater. Horiz.*, 2018, **5**, 9–27.
8 H. Ali, M. Masar, A. C. Guler, M. Urbanek, M. Machovsky and I. Kuritka, *Nanoscale Adv.*, 2021, **3**, 6358–6372.
9 Y. Chen, M. Wen and Q. Wu, *CrystEngComm*, 2011, **13**, 3035.
10 H. An, Y. Du, T. Wang, C. Wang, W. Hao and J. Zhang, *Rare Met.*, 2008, **27**, 243–250.
11 L. Zhang, X.-F. Cao, X.-T. Chen and Z.-L. Xue, *J. Colloid Interface Sci.*, 2011, **354**, 630–636.
12 M. Banoo, K. Samanta, A. K. Sah, R. S. Roy, M. Bhakar, D. Sanyal, D. G. Porob, K. Glazyrin, D. Topwal, G. Sheet, D. Ghosh and U. K. Gautam, *Adv. Funct. Mater.*, 2024, **34**, 2411464.
13 J. Li, L. Cai, J. Shang, Y. Yu and L. Zhang, *Adv. Mater.*, 2016, **28**, 4059–4064.
14 A. Han, J. Sun, G. K. Chuah and S. Jaenicke, *RSC Adv.*, 2017, **7**, 145–152.
15 J. Huang, C. Li, H. Hao, L. Li, B. Zhu, X. Chen and H. Tao, *Front. Nanotechnol.*, 2022, **4**, 1023489.
16 S. S. Imam, R. Adnan and N. H. Mohd Kaus, *J. Environ. Chem. Eng.*, 2021, **9**, 105404.
17 F. Chang, C. Li, J. Chen, J. Wang, J. Luo, Y. Xie, B. Deng and X. Hu, *Superlattices Microstruct.*, 2014, **76**, 90–104.
18 R. Kumar, S. K. Jena, M. M. Habtegbrel, R. Gogoi, A. Singh and P. F. Siril, *ChemistrySelect*, 2025, **10**, e202405902.
19 X. Cheng, X. Xiao, F. Wang, T. Lu and Y. Zhang, *ACS Appl. Nano Mater.*, 2024, **7**, 4413–4422.
20 Z. Shi, Y. Zhang, G. Duoerkun, W. Cao, T. Liu, L. Zhang, J. Liu, M. Li and Z. Chen, *Environ. Sci.: Nano*, 2020, **7**, 2708–2722.
21 P. Li, S. Gao, Q. Liu, P. Ding, Y. Wu, C. Wang, S. Yu, W. Liu, Q. Wang and S. Chen, *Adv. Energy Sustain. Res.*, 2021, **2**, 2000097.
22 X. Zheng, X. Wang, L. Feng, Z. Chen, J. Zhang, X. Zhang and P. Liu, *ACS Appl. Mater. Interfaces*, 2024, **16**, 62107–62120.
23 M. Cheng, C. Xiao and Y. Xie, *J. Mater. Chem. A*, 2019, **7**, 19616–19633.
24 C. Tedesco, L. Gregori, A. Simbula, F. Pitzalis, A. Speltini, F. Merlo, S. Colella, A. Listorti, E. Mosconi, A. A. Alothman, W. Kaiser, M. Saba, A. Profumo, F. De Angelis and L. Malavasi, *Adv. Energy Sustain. Res.*, 2024, 2400040.
25 C. Tedesco, A. Simbula, R. Pau, F. Merlo, A. Speltini, V. Armenise, A. Listorti, L. Gregori, A. A. Alothman, E. Mosconi, M. Saba, A. Profumo and L. Malavasi, *Sol. RRL*, 2025, **9**, 2400778.
26 X. Yang, D. Cui, T. Zhang, Y. Liu and F. Li, *Inorg. Chem. Front.*, 2024, **11**, 8246–8257.
27 K. Gao, C. Zhang, H. Zhu, J. Xia, J. Chen, F. Xie, X. Zhao, Z. Tang and X. Wang, *Chem. – Eur. J.*, 2023, **29**, e202300616.
28 S. Chandrappa, S. J. Galbao, A. Furube and D. H. K. Murthy, *ACS Appl. Nano Mater.*, 2023, **6**, 19551–19572.
29 Z.-Y. Zhao, Q.-L. Liu and W.-W. Dai, *Sci. Rep.*, 2016, **6**, 31449.
30 Y. Zhao, R. Shi, X. Bian, C. Zhou, Y. Zhao, S. Zhang, F. Wu, G. I. N. Waterhouse, L. Wu, C. Tung and T. Zhang, *Adv. Sci.*, 2019, **6**, 1802109.
31 K. Akaike, K. Aoyama, S. Dekubo, A. Onishi and K. Kanai, *Chem. Mater.*, 2018, **30**, 2341–2352.
32 E. Alwin, W. Nowicki, R. Wojcieszak, M. Zieliński and M. Pietrowski, *Dalton Trans.*, 2020, **49**, 12805–12813.
33 Y. Zhang, J. Chen, W. Lin, R. Gao, X. Mai, H. Lin and Y. He, *CrystEngComm*, 2024, **26**, 6729–6738.
34 H. Ouhbi and J. Wiktor, *J. Phys. Chem. C*, 2022, **126**, 19956–19961.
35 G. Miceli, W. Chen, I. Reshetnyak and A. Pasquarello, *Phys. Rev. B*, 2018, **97**, 121112.
36 T. Bischoff, I. Reshetnyak and A. Pasquarello, *Phys. Rev. B*, 2019, **99**, 201114.
37 T. Bischoff, J. Wiktor, W. Chen and A. Pasquarello, *Phys. Rev. Mater.*, 2019, **3**, 123802.
38 L. Romani, A. Speltini, F. Ambrosio, E. Mosconi, A. Profumo, M. Marelli, S. Margadonna, A. Milella, F. Fracassi, A. Listorti, F. De Angelis and L. Malavasi, *Angew. Chem., Int. Ed.*, 2021, **60**, 3611–3618.
39 T. Fu, H. Zhang, L. Wang, T. Zhang, J. Sun, K. Liu, L. Guo, P. Wang and S. Zhan, *Chem. Eng. J.*, 2024, **502**, 157919.
40 L. Yu, H. Li, H. Shang, P. Xing, B. Zhou, Z. Chen, X. Liu, H. Zhang, Y. Shi and L. Zhang, *ACS Nano*, 2023, **17**, 15077–15084.
41 J. Heyd, G. E. Scuseria and M. Ernzerhof, *J. Chem. Phys.*, 2003, **118**, 8207–8215.
42 J. Heyd, G. E. Scuseria and M. Ernzerhof, *J. Chem. Phys.*, 2006, **124**, 219906.
43 J. Wiktor, I. Reshetnyak, F. Ambrosio and A. Pasquarello, *Phys. Rev. Mater.*, 2017, **1**, 022401.
44 Y. Q. Gao, Y. Georgievskii and R. A. Marcus, *J. Chem. Phys.*, 2000, **112**, 3358–3369.
45 F. Ambrosio, G. Miceli and A. Pasquarello, *J. Chem. Phys.*, 2015, **143**, 244508.
46 F. Ambrosio, G. Miceli and A. Pasquarello, *J. Phys. Chem. Lett.*, 2017, **8**, 2055–2059.
47 L. Romani, A. Speltini, C. N. Dibenedetto, A. Listorti, F. Ambrosio, E. Mosconi, A. Simbula, M. Saba, A. Profumo, P. Quadrelli, F. De Angelis and L. Malavasi, *Adv. Funct. Mater.*, 2021, **31**, 2104428.
48 F. Ambrosio and J. Wiktor, *Appl. Phys. Lett.*, 2025, **126**, 130501.
49 F. Ambrosio, D. Meggiolaro, E. Mosconi and F. De Angelis, *J. Mater. Chem. A*, 2020, **8**, 6882–6892.
50 D. Ricciarelli, E. Mosconi, J. Wiktor, L. Malavasi, F. Ambrosio and F. D. Angelis, *Int. J. Hydrogen Energy*, 2024, **58**, 863–871.
51 D. Ricciarelli, W. Kaiser, E. Mosconi, J. Wiktor, M. W. Ashraf, L. Malavasi, F. Ambrosio and F. De Angelis, *ACS Energy Lett.*, 2022, **7**, 1308–1315.
52 X. Wu, Y. H. Ng, L. Wang, Y. Du, S. X. Dou, R. Amal and J. Scott, *J. Mater. Chem. A*, 2017, **5**, 8117–8124.

Open Access Article. Published on 04 February 2026. Downloaded on 4/9/2026 3:41:24 PM.
This article is licensed under a Creative Commons Attribution-NonCommercial 3.0 Unported Licence.

53 Y. Li, D. Wang, J. Liu, L. Wang, H. Wang, S. Wang, B. Wu and M. Liu, *Appl. Surf. Sci.*, 2025, **688**, 162446.
54 J. Li, K. Zhao, Y. Yu and L. Zhang, *Adv. Funct. Mater.*, 2015, **25**, 2189–2201.
55 J. Geng, Y. Cao, H. Fu, J. Chang, H. Gao, F. Liao, J. Zhang and Y. Liao, *Sol. Energy*, 2025, **300**, 113863.
56 J. Wang, L. Zhang, Y. Hu, X. Du, X. Hao, Q. Cao, G. Guan, Z. Liu, J. Li, S. Luo and X. An, *Chem. Eng. J.*, 2023, **460**, 141798.
57 L. Xia, H. Chen, W. Wang, X. Jia, D. Zhang, L. Wang, P. Wu, L. Li and J. Huang, *J. Mater. Sci. Technol.*, 2024, **202**, 39–49.
58 J. H. Noh, S. H. Im, J. H. Heo, T. N. Mandal and S. I. Seok, *Nano Lett.*, 2013, **13**, 1764–1769.
59 H. Ouhbi, F. Ambrosio, F. De Angelis and J. Wiktor, *J. Phys. Chem. Lett.*, 2021, **12**, 5339–5343.
60 Y. Wang, C. Liu, X. Liu, J. Han, L. Yang, X. Liao and Y. Yao, *Appl. Surf. Sci.*, 2025, **710**, 163963.

This journal is © The Royal Society of Chemistry 2026